Development of a ReaxFF potential for Pd/O and application to palladium oxide formation

Thomas P. Senftle, Randall J. Meyer, Michael J. Janik, and Adri C. T. van Duin

Citation: The Journal of Chemical Physics **139**, 044109 (2013); doi: 10.1063/1.4815820
View online: http://dx.doi.org/10.1063/1.4815820
View Table of Contents: http://scitation.aip.org/content/aip/journal/jcp/139/4?ver=pdfcov
Published by the AIP Publishing

Development of a ReaxFF potential for Pd/O and application to palladium oxide formation

Thomas P. Senftle,[1] Randall J. Meyer,[2] Michael J. Janik,[1,a)] and Adri C. T. van Duin[3,a)]
[1]*Department of Chemical Engineering, Pennsylvania State University, University Park, Pennsylvania 16802, USA*
[2]*Department of Chemical Engineering, University of Illinois at Chicago, Chicago, Illinois 60607, USA*
[3]*Department of Mechanical and Nuclear Engineering, Pennsylvania State University, University Park, Pennsylvania 16802, USA*

(Received 25 March 2013; accepted 2 July 2013; published online 25 July 2013)

Oxide formation on palladium surfaces impacts the activity and selectivity of Pd-based catalysts, which are widely employed under oxygen rich operating conditions. To investigate oxidation processes over Pd catalysts at time and length scales inaccessible to quantum based computational methods, we have developed a Pd/O interaction potential for the ReaxFF reactive force field. The parameters of the ReaxFF potential were fit against an extensive set of quantum data for both bulk and surface properties. Using the resulting potential, we conducted molecular dynamics simulations of oxide formation on Pd(111), Pd(110), and Pd(100) surfaces. The results demonstrate good agreement with previous experimental observations; oxygen diffusion from the surface to the subsurface occurs faster on the Pd(110) surface than on the Pd(111) and Pd(100) surfaces under comparable conditions at high temperatures and pressures. Additionally, we developed a ReaxFF-based hybrid grand canonical Monte Carlo/molecular dynamics (GC-MC/MD) approach to assess the thermodynamic stability of oxide formations. This method is used to derive a theoretical phase diagram for the oxidation of Pd_{935} clusters in temperatures ranging from 300 K to 1300 K and oxygen pressures ranging from 10^{-14} atm to 1 atm. We observe good agreement between experiment and ReaxFF, which validates the Pd/O interaction potential and demonstrates the feasibility of the hybrid GC-MC/MD method for deriving theoretical phase diagrams. This GC-MC/MD method is novel to ReaxFF, and is well suited to studies of supported-metal-oxide catalysts, where the extent of oxidation in metal clusters can significantly influence catalytic activity, selectivity, and stability. © *2013 AIP Publishing LLC*. [http://dx.doi.org/10.1063/1.4815820]

I. INTRODUCTION

Catalytic applications featuring late transition metals often employ oxygen rich operating conditions that are capable of oxidizing the metal catalyst. This leads to the formation of surface and bulk oxide phases with catalytic properties that differ greatly from the parent metal.[1–7] This is particularly important in palladium-based systems, which are well known oxidation catalysts used industrially for automotive exhaust treatment,[8–10] CO conversion to CO_2,[11–17] and hydrocarbon oxidation.[17–21] To optimize catalyst performance, it is necessary to understand the stability of oxide surface phases as a function of temperature, pressure, and gas phase composition, as well as the dynamic transition between oxide phases that may occur during catalytic operation.

Numerous experimental and theoretical studies have characterized oxide formation on Pd single-crystal surfaces.[1,7,22–33] Intuitively, oxide formation typically occurs after the initial adsorption and dissociation of oxygen molecules on the surface, followed by the growth of two-dimensional surface oxides, and the subsequent formation of a bulk oxide. The extent of oxidation on the surface and in the bulk is governed by both kinetic and thermodynamic influences. Lundgren *et al.*[22] combined *in situ* surface x-ray diffraction with *ab initio* thermodynamics to demonstrate that, on the Pd(100) surface, both a $p(2 \times 2)$ adsorbate phase and a 2D $(\sqrt{5} \times \sqrt{5})R27^\circ$ surface oxide phase can be kinetically stable, and that their presence on the surface hinders the formation of the thermodynamically favored bulk oxide. Similarly, Salmeron and co-workers compared theoretical and experimental phase diagrams of Pd(111) derived from *ab inito* thermodynamics and photoemission spectroscopy to demonstrate the kinetic stability of a subsurface oxide phase that prevents further oxidation of the bulk.[28] Recently, Westerström *et al.*[31] utilized *in situ* x-ray diffraction and density functional theory (DFT) to demonstrate that bulk oxidation on Pd(110) does *not* proceed through a kinetically stable surface phase, resulting in rapid bulk oxidation compared to other low-index Pd surfaces. Using a combination of scanning tunneling microscopy (STM), low energy electron diffraction (LEED), and temperature programmed decomposition (TPD), Han *et al.*[34,35] observed a similar trend in affinity toward oxide formation over Pd single crystal surfaces: Pd(110) > Pd(100) > Pd(111). Since catalytic behavior is strongly impacted by the extent of oxidation on the surface and in the bulk, these findings underscore the necessity to thoroughly investigate both

a)Authors to whom correspondence should be addressed. Electronic addresses: mjanik@engr.psu.edu and acv13@engr.psu.edu

kinetic and thermodynamic influences when characterizing oxide formation. This has motivated the work presented here, in which we have developed an empirical reactive force-field (ReaxFF) for Pd/O that, through molecular dynamics (MD) and Monte Carlo (MC) simulations, can help examine oxidization processes on the atomic scale.

Atomistic modeling is a useful method for analyzing the kinetic and thermodynamic properties of oxidation processes during catalytic operation.[1,36–38] The studies mentioned above illustrate how quantum results can be extended to describe ambient conditions through the formalism of *ab initio* thermodynamics.[23,32,39] Unfortunately, the computational expense inherent to quantum mechanical simulations limits such studies to small (∼100 atoms) and highly idealized (periodic) system models. It also precludes direct dynamic studies, as *ab initio* MD is limited to ∼fs-ps timescales. Alternatively, empirical force-field methods offer a computationally inexpensive means for modeling processes that occur over larger length and time scales. Although still unable to reach macroscopic time and length scales, these methods can help bridge the size gap between experimental and theoretical studies.

Empirical force-field methods feature inter-atomic potentials that contain parameters optimized against experimental or quantum data. The ReaxFF force-field used here incorporates bond order descriptions in the inter-atomic potential to capture the reaction energetics of covalent interactions. This eliminates pre-defined atomic connectivities required in non-reactive force fields, enabling the potential to describe bond dissociation and formation during reactive events. The viability of bond-length/bond-order based force-fields was initially demonstrated by Tersoff for Si-based systems[40] and by Brenner for hydrocarbon systems.[41] ReaxFF incorporates an extended bond-length/bond-order formalism to better describe long range covalent interactions characteristic in transition state structures, allowing the force-field to describe reaction barriers. This was initially demonstrated through application to hydrocarbon systems,[42,43] and has since been expanded to include metals[44–52] and oxides.[53–58] The transferability of ReaxFF makes it a logical choice for studying oxidation processes; it can describe O_2 adsorption from the gas phase, dissociation on the metal surface, and diffusion into the bulk metal. Herein we derive and validate ReaxFF parameters for describing the interaction between palladium and oxygen in gas, surface, and bulk phases. We apply the resulting potential in MD and Monte Carlo simulations of the oxidation process, which involves oxygen migration between gas, surface, and bulk phases.

Though MD methods are useful for modeling the dynamics of oxide formation, they are often unable to reach thermodynamic equilibrium within computationally tractable time scales (∼1 ns for ReaxFF). Simulations at high temperatures and pressures can overcome kinetic barriers in shorter timescales, but will allow high energy processes that are not thermodynamically feasible under ambient conditions. Monte Carlo methods can circumvent this limitation by sampling the configurational energetics of the system and reproducing a Boltzmann thermal distribution of states that fluctuate around thermodynamic equilibrium. In particular, grand canonical Monte Carlo (GC-MC) methods are aptly suited to model the thermodynamics of sorption processes.[59–63] In such simulations, atoms are stochastically exchanged between the system and a gas phase reservoir at constant chemical potential. The system equilibrates when the chemical potential of the system is equal to that of the gas phase reservoir, thus determining the equilibrium concentration of sorbate atoms and the corresponding phase structure. This method is used in this work to derive a theoretical oxidation phase diagram in *T*,*P* space for large $Pd_{n>300}$ clusters, which is beyond the computational expense of *ab initio* methods.

GC-MC studies have been conducted previously to model sorption in multi-component systems. Ray and co-workers demonstrated the multi-component GC-MC method, in which atoms are exchanged between a gas phase reservoir and a metal lattice, in their work modeling Pd bulk[61] and Pd clusters.[60,62] A similar study was conducted by Debiaggi and co-workers,[64] demonstrating the formation of a PdH subsurface phase prior to the formation of a bulk hydride in Pd nanoclusters. Additionally, Valentini *et al.* employed GC-MC via ReaxFF to investigate oxygen adsorption on the Pt(111) surface.[65] The direct GC-MC methods employed in these studies, however, cannot be applied to model bulk oxidation because the transition from pure metal to bulk metal-oxide requires a significant rearrangement of the metal lattice. Hybrid Monte Carlo techniques offer a solution to this issue by combining MC configuration steps with a MD relaxation of forces.[66–70] Hybrid-MC/MD was first implemented in ReaxFF by Chenoweth *et al.*,[70] who employed atom swaps in an NVT ensemble to investigate the structure of molybdenum-doped vanadium oxide surfaces. Building on this method, we have developed a hybrid GC-MC/MD method for ReaxFF that uses GC-MC to add, remove, and move oxygen atoms until thermodynamic equilibrium with an oxygen reservoir is reached, and uses MD to relax the system as oxygen atoms are incorporated in the metal lattice in both surface and bulk sites. This scheme is capable of modeling structural rearrangements inherent to the formation of the oxide. Although the GC-MC/MD methodology presented in Secs. II A–II D is tailored to oxidation processes, the formalism is generally applicable to other multi-component systems.

II. THEORY AND METHODS

A. ReaxFF background

ReaxFF utilizes bond-order/bond-length relationships in conjunction with polarizable charge descriptions to describe covalent, Coulomb, and van der Waals interactions between atoms. The general form of the ReaxFF potential is shown below:

$$E_{system} = E_{bond} + E_{val} + E_{tors} + E_{over} + E_{under} + E_{vdWaals} + E_{Coulomb}, \quad (1)$$

where E_{system} is the total potential energy of the system. E_{bond} describes the energy associated with forming covalent bonds between atoms; E_{val} and E_{tors} are the energies associated with three-body valence angle strain and four-body torsional angle strain. These terms are a function of bond-order, which is in

turn calculated from inter-atomic distance using the equation:

$$BO_{ij} = BO_{ij}^{\sigma} + BO_{ij}^{\pi} + BO_{ij}^{\pi\pi} = \exp\left[p_{bo1}\left(\frac{r_{ij}}{r_o^{\sigma}}\right)^{p_{bo2}}\right] + \exp\left[p_{bo3}\left(\frac{r_{ij}}{r_o^{\pi}}\right)^{p_{bo4}}\right] + \exp\left[p_{bo5}\left(\frac{r_{ij}}{r_o^{\pi\pi}}\right)^{p_{bo6}}\right], \quad (2)$$

where BO is the bond-order between atoms i and j, r_{ij} is inter-atomic distance, r_o terms are equilibrium bond lengths, and p_{bo} terms are empirical parameters. Equation (2) is a continuous function of inter-atomic distance, and contains no discontinuities through transitions between σ, π, and $\pi\pi$ bond character. This yields a differentiable potential energy surface, which is required for the direct calculation of inter-atomic forces. E_{over} and E_{under} are energy penalties that prevent the over and under coordination of atoms based on atomic valences. $E_{Coulomb}$ and $E_{vdWaals}$ are electrostatic and dispersive interactions, respectively, calculated between all atom pairs regardless of connectivity. These two terms are bond-order independent and are calculated directly from inter-atomic distances. Electrostatic interactions are described via a variable-charge electrostatic description that computes the partial charge of individual atoms from a self-consistent electron equilibration method (EEM).[71] The exact functional forms of each term in the ReaxFF potential are described in detail in a previous publication.[42] In this study, system-specific parameters contained in the ReaxFF potential were optimized against a DFT training set populated with bulk, surface, and gas phase data for palladium and oxygen. The optimization technique consisted of a previously developed[72,73] single-parameter error minimization scheme. The parameter optimization process for Pd/O systems is fully described in Sec. III.

B. ReaxFF grand canonical Monte Carlo

Using the Pd/O potential, we implemented a hybrid GC-MC/MD method in the $TV\mu_{O_2}N_{Pd}$ ensemble with constant temperature (T), volume (V), oxygen chemical potential (μ_{O_2}), and number of Pd atoms (N_{Pd}). Possible MC moves include: (1) inserting an oxygen atom into the system at a random position, (2) removing a randomly selected oxygen atom from the system, or (3) moving an oxygen atom to a new random position in the system. Coordinates for O-insertion and O-move steps were chosen randomly such that any unoccupied position in the simulation box could be selected. At equilibrium, the Monte Carlo procedure must maintain a detail-balance, in which the probability of any transition is equal to the probability of the reverse transition.[63,74,75] This is demonstrated in the probability balance:

$$P_1^{Boltz} P_{1\to2}^{select} P_{1\to2}^{accept} = P_2^{Boltz} P_{2\to1}^{select} P_{2\to1}^{accept}, \quad (3)$$

where P^{Boltz} is the Boltzmann probability that a microstate is occupied, P^{select} is the probability that a transition type is selected, and P^{accept} is the probability that the transition is accepted. In the above equation, we ensure that P^{select} is equal on both sides by generating move types with an equal frequency. The probability of accepting a MC step is derived from the remaining Boltzmann terms, yielding the following acceptance criteria for particle insertion, deletion, or displacement during a Monte Carlo transition:

$$P_{insert}^{accept} = min\left[1, \frac{V}{\Lambda^3 (N+1)}\exp[-\beta(E_2 - E_1 - \mu_{res})\right], \quad (4)$$

$$P_{remove}^{accept} = min\left[1, \frac{N\Lambda^3}{V}\exp[-\beta(E_2 - E_1 + \mu_{res})\right], \quad (5)$$

$$P_{move}^{accept} = min\left[1, \exp[-\beta(E_2 - E_1)\right], \quad (6)$$

where N is the number of exchangeable particles in the system before the MC move, V is the volume of the system, Λ is the thermal de Broglie wavelength of the exchanged particle, β is the Boltzmann factor given by $\beta = 1/k_bT$, E_1 and E_2 are the potential energies calculated as a function of particle configurations in the system before and after the MC move, and μ_{ref} is the chemical potential of the particle reservoir. In this study, μ_{ref} for oxygen is related to T and P by the following equation:

$$\mu_O(T, P) = \frac{1}{2}\mu_{O_2}(T, P) = \frac{1}{2}\left[\mu_{ref}(T, P^o) + k_bT \ln\left(\frac{P}{P^o}\right) - E_d\right], \quad (7)$$

where $\mu_{O_2}(T,P^o)$ is the experimentally determined chemical potential of O_2 at T and P^o available from published thermodynamic tables,[76] and E_d is the zero-Kelvin bond dissociation energy of O_2. Since the ReaxFF parameters are derived from DFT values for oxygen adsorption calculated relative to gas phase O_2, the DFT calculated value of 142.1 kcal mol^{-1} was used for E_d to remain consistent with the ReaxFF training, despite the well documented DFT overestimation of the O_2 bond strength. Using the DFT value for E_d introduces uncertainty in the location of the oxidation phase boundaries determined from MC. We estimate that DFT errors in O_2 binding could shift the resultant oxidation boundaries to lower temperatures by as much as ~200 K and to higher pressures by as much as an order of magnitude. This uncertainty should be taken into account for quantitative comparisons with experiment, but does not affect qualitative conclusions drawn from the results.

In our hybrid method, we introduce an energy minimization step after each MC trial move. This step is necessary to allow the rearrangement of metal atoms when forming an oxide. Pure GC-MC simulations of solid-oxide formation without an energy minimization step will suffer from low acceptance rates because the majority of the system is occupied by metal atoms and is inaccessible to inserted oxygen atoms. An energy minimization step will alleviate this issue by relaxing the energy of the system prior to applying Eqs. (4)–(6), but will introduce a bias in the MC algorithm that must be accounted for in the acceptance probabilities to maintain detail-balance. This was demonstrated by Lachet *et al.*,[63] who employed a biased GC-MC method to simulate the adsorption of

xylene molecules in zeolites. They demonstrate that the bias introduced by the energy minimization step can be countered by replacing the system volume, V, in Eqs. (4) and (5) with an *accessible* volume, V_{acc}, which reflects the volume accessible to the MC-inserted atom. Herein, the accessible volume is calculated by subtracting the volume occupied by Pd metal atoms from the total volume:

$$V_{acc} = V - N_{metal}\frac{4}{3}\pi r_{metal}^3, \tag{8}$$

where N_{metal} is the number of metal atoms and r_{metal} is the atomic radius of the metal atom (for Pd, $r_{metal} = 1.39$ Å). In this study, the energy minimization step consists of a conjugant gradient (CG) geometry optimization, with a convergence criterion of 0.5 kcal mol^{-1} between subsequent CG steps. The convergence criterion affects the accessible volume, since the CG algorithm determines how close an inserted O atom can be placed to any Pd atom. In the limit of an extremely loose criterion, an inserted O atom can be placed within the atomic radii of the Pd atoms, resulting in larger accessible volumes and lower MC acceptance rates as these structures would be very high in energy. Conversely, employing a tight convergence criterion will decrease the accessible volume, but will increase the computational expense of each MC trial move. The 0.5 kcal mol^{-1} convergence criterion was chosen because it provides a reasonable tradeoff, in which the CG converges in a reasonable timeframe, while still preventing inserted O atoms from being placed in high energy regions within the atomic radius of a Pd atom. We tested tighter and looser convergence criteria, which impacted the computational time required for the MC run to reach equilibrium, but did not significantly impact the final equilibrium values.

The final MC algorithm consists of the following steps: (1) execute MC move, (2) relax atomic forces by conjugate gradient energy minimization, (3) accept or reject the MC move and geometry resulting from relaxation using Eqs. (4)–(6) above, and (4) iterate until the system energy converges at equilibrium. The converged system reflects the formation of an oxide in equilibrium with a gas phase at the temperature and pressure specified by the reference chemical potential, $\mu_{ref}(T, P)$.

C. ReaxFF molecular dynamics

MD simulations in this study were conducted in the NVT ensemble using the velocity Verlet method[77] with a time step of 0.25 fs. Temperature control was maintained using a Berendsen thermostat[78] with a damping constant of 100 fs. Energy minimization via a conjugate gradient relaxation of forces was conducted prior to each MD run to eliminate simulation artifacts that can arise from high energy contacts initially present in the starting geometry.

D. QM method

Density functional calculations were completed in the Vienna *ab initio* simulation package (VASP).[79,80] The exchange-correlation functional was treated with the Perdew-Wang (PW91) version of the generalized gradient approximation (GGA).[81] Atomic core regions were represented using the projector augmented wave method,[82] with valence configurations of $4d^{10}$ for Pd atoms and $2s^2 2p^4$ for O atoms. Plane-wave basis sets were truncated at 400 eV for surface calculations and 600 eV for bulk structures. A convergence criterion of atomic forces less than 0.05 eV Å^{-1} was employed for all structural optimizations. The Monkhorst-Pack (MP) formulation[83] was used to sample the Brillouin zone of all periodic calculations. A $7 \times 7 \times 1$ MP k-point spacing was used for Pd surface calculations in a $2 \times 2 \times 6$ periodic cell including a 15 Å vacuum layer between periodic images in the z-direction perpendicular to the surface. The bottom three Pd layers were held fixed during structural optimizations to simulate the underlying bulk. A $6 \times 6 \times 6$ MP k-point spacing was used for bulk Pd and PdO, where minimal orthogonal unit cells were employed. Clusters were modeled in a 45 Å $\times$ 45 Å $\times$ 45 Å periodic box with the gamma point considered. Transition states for oxygen dissociation were identified using the climbing image nudged elastic band (CI-NEB) procedure as implemented in VASP,[84] and were conducted in a $3 \times 3 \times 6$ periodic cell to minimize adsorbate-adsorbate interactions across periodic images.

III. RESULTS AND DISCUSSION

A. Force field development

1. Palladium-palladium metal interactions

The Pd atom and Pd–Pd interaction parameters listed in Table I were obtained by optimizing the ReaxFF potential against a training set of 85 data points consisting of both bulk and surface DFT data. We first optimized bulk formation energies calculated as a function of lattice compression and expansion for fcc, bcc, simple cubic, and diamond structure phases of Pd. This enables the potential to properly describe bulk Pd–Pd interactions in numerous configurations and chemical environments. Energetically unfavorable phases that are not experimentally viable, such as simple cubic and diamond, were included in the training to ensure that the potential will not improperly favor these high energy phases. The resulting expansion-compression energy curves, shown in Figure 1, demonstrate that the potential correctly discerns energy differences separating bulk Pd phases. ReaxFF predicts that the bcc phase is 1.61 kcal mol^{-1} higher in energy than the fcc phase, which agrees with the DFT value of 0.92 kcal mol^{-1}. The potential yields cubic and diamond phases that are 19.43 and 28.19 kcal mol^{-1} higher in energy, respectively, compared to the fcc phase, in reasonable agreement with the respective DFT values of 11.06 kcal mol^{-1} and 21.91 kcal mol^{-1}. Agreement between DFT and ReaxFF for high energy phases and at densities far from equilibrium is less important for capturing correct Pd–Pd interaction behavior, as long as these phases and densities are unrealizable under relevant simulation conditions. Finally, the potential yields a cohesion energy of -87.7 kcal mol^{-1}, in agreement with the DFT value of -89.8 kcal mol^{-1}, and the experimental value of -89.7 kcal mol^{-1}.[85,86]

The expansion-compression curves in Figure 1 can be used to determine structural properties that are directly

TABLE I. ReaxFF parameters optimized from 85 point DFT training set for Pd–Pd terms and 48 point set for Pd–O (units: r and γ terms in Å; ε, D, k, and V in kcal mol^{-1}; η and χ in eV; θ in degrees; all other terms are dimensionless).

Atom	r_o	η	χ	γ	r_{vdW}	ε_{vdw}	α	γ_{vdW}
Pd	1.8582	6.6477	5.5005	1.0000	2.0113	0.2465	12.5712	6.0083
O[a]	1.245	8.3122	8.5000	1.0898	2.389	0.1000	9.7300	13.8449
Bond	D_e^σ	$p_{be,1}$	$p_{ovun,1}$	$p_{be,2}$	$p_{bo,1}$	$p_{bo,2}$		
Pd–Pd	90.7003	−0.1661	0.2578	3.0618	−0.0914	5.4665		
Pd–O	56.7412	0.7149	0.1000	11.9839	−0.3000	4.7089		
Off-diagonal	r^σ	R_{vdW}	γ	ε^σ				
Pd–O	1.7139	1.661	10.6568	0.2237				
Valence angle	θ_o	k_a	k_b	$p_{val,2}$				
Pd–Pd–O	55.7429	4.8907	3.9242	1.0000				
Pd–O–Pd	53.8540	30.0000	2.0649	1.7008				
O–Pd–O	0.0100	30.0000	8.0000	2.4156				
Pd–O–O	90.0000	30.0000	1.6813	1.9155				
Torsion angle	V_1	V_2	V_3	$P_{tor,1}$	$P_{tor,2}$			
Pd–O–O–Pd	1.7276	50.0000	0.0100	−2.5000	−1.0000			

[a]Oxygen atom parameters from Ref. 92.

comparable with experimental results, such as the fcc lattice constant, the density, and the bulk modulus of Pd metal. The ReaxFF potential predicts an equilibrium lattice constant of 3.97 Å for the fcc phase, which is in good agreement with the respective DFT and experimental[87] values of 3.95 Å and 3.89 Å. The ReaxFF lattice spacing yields a density of 11.3 g/cm^3, in agreement with the experimental[86,87] value of 12.0 g/cm^3. The bulk modulus of fcc Pd can be determined from the expansion-compression curve using the Birch-Murnaghan equation of state for crystalline solids,[88] as shown in the insets of Figure 1. A least squares regression of the third order Birch-Murnaghan equation yields a bulk modulus of 140.1 GPa from the ReaxFF data and 144.2 GPa from the DFT data. Both of these values are in reasonable agreement with the experimental value of 180.8 GPa.[86,87] The above comparisons between ReaxFF, DFT, and experiment are summarized in Table II.

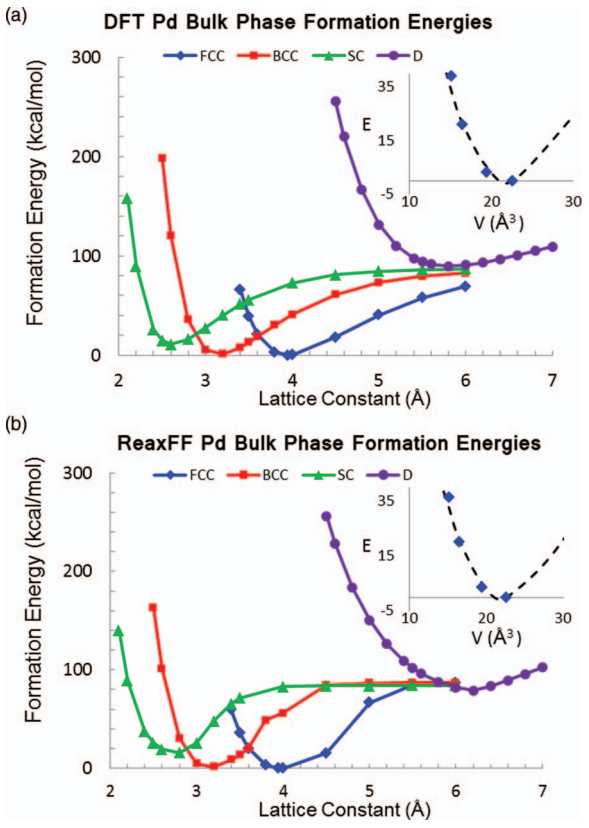

FIG. 1. (a) DFT and (b) ReaxFF expansion-compression curves for fcc, bcc, simple cubic, and diamond structures of bulk Pd. (Insets) Birch-Murnaghan equation of state fit to the minima of the DFT and ReaxFF bulk fcc curves.

Pd–Pd interaction parameters were also optimized to reproduce DFT surface energies for Pd(111) and Pd(100) surfaces. Surface energies for converged 12-layer slab models normalized by the number of surface atoms, calculated with the formula: $\sigma_{surf} = 1/2\ (E_{slab,n} - n\ E_{bulk})$, are shown in Table III, along with literature comparisons. For Pd(111), Pd(100), and Pd(110), ReaxFF predicts surface energies of 10.71 kcal mol^{-1}, 13.95 kcal mol^{-1}, and 20.77 kcal mol^{-1}, respectively, in reasonable agreement with our respective DFT values of 12.97 kcal mol^{-1}, 17.44 kcal mol^{-1}, and 25.26 kcal mol^{-1}. The results are also in agreement with the previously reported DFT values of 12.91 kcal mol^{-1}, 17.06 kcal mol^{-1}, and 24.91 kcal mol^{-1}.[89] Despite having not been explicitly optimized against data for the Pd(110) surface, ReaxFF is in qualitative agreement with DFT and literature results for this surface, predicting Pd(110) to be significantly higher in energy than the Pd(100) surface and Pd(111) surfaces.

The Pd–Pd training set contains structures that sample a range of chemical environments, thus allowing the potential to

TABLE II. Properties of bulk-fcc Pd metal from ReaxFF, DFT, and experiment.

Property	ReaxFF	DFT	Experimental
Lattice constant (Å)	3.97	3.95	3.89[86,87]
Density (g/cm^3)	11.3	11.5	12.0[86,87]
Bulk modulus (GPa)	140.1	144.2	180.8[86,87]
Cohesion energy (kcal mol^{-1})	−87.7	−89.8	−89.7[85,86]
Vacancy energy (kcal mol^{-1})	41.1	29.8	32.3[90,91]

TABLE III. Pd surface energies (per surface Pd atom).

Surface	ReaxFF (kcal mol^{-1})	DFT (kcal mol^{-1})	Literature DFT (kcal mol^{-1})
111	10.71	12.97	12.91[89]
100	13.95	17.44	17.06[89]
110	20.77	25.26	24.91[89]

describe Pd–Pd interactions in structures that are not explicitly considered during parameter training. Figure 2 contains relative DFT and ReaxFF cluster energies for Pd_n clusters with n ranging from 6 to 236 atoms, where the relative cluster energy was calculated using the formula: $E_{rel} = E_{cluster,n}/n - E_{bulk}$. Although these structures were not contained in the training set, the potential performs well, yielding energies within ~5 kcal mol^{-1} of the DFT value for cluster sizes larger than 48 atoms and within ~3 kcal mol^{-1} for clusters larger than 135 atoms. Larger deviations occur for smaller clusters, with a deviation of ~7 kcal mol^{-1} for cluster sizes between 19 and 43 atoms. The large deviation of ~12 kcal mol^{-1} for the 6 atom cluster demonstrates the limitation of the ReaxFF potential for describing small ($n < 15$) gas phase clusters. For this reason, we restrict our analysis in the following sections to cluster sizes larger than 43 atoms. In addition to cluster formation, we compared the performance of ReaxFF for describing the formation of vacancies in the fcc lattice, which was not included in the parameter fitting process. The potential yields a vacancy formation energy of 41.1 kcal mol^{-1}, in reasonable agreement with the DFT value of 29.8 kcal mol^{-1} and the empirical value of 33.21 kcal mol^{-1} (estimated from the experimental melting point of Pd metal[90,91]). These comparisons demonstrate the strengths and limitations of the Pd–Pd potential for describing both surface and bulk properties in structures that are not present in the 85 point training set described above.

2. Palladium-oxygen interactions

A 49 point DFT training set consisting of bulk, surface, and adsorption data was used to optimize the Pd–O interaction parameters shown in Table I. The oxygen atom and O–O interaction parameters were derived in a previous study.[92]

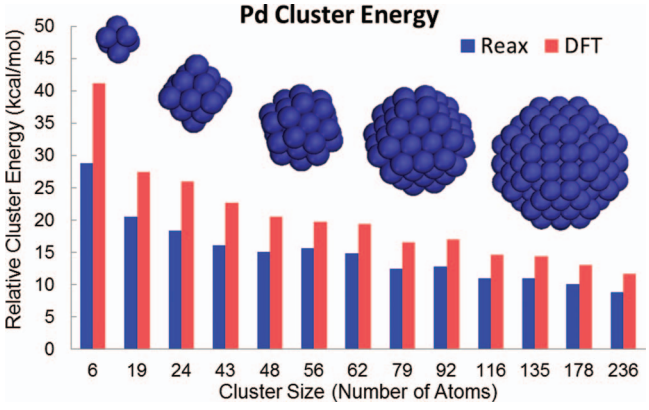

FIG. 2. ReaxFF and DFT cluster energies per Pd atom relative to the fcc bulk. (Insets) Structures of 6, 24, 48, 92, and 236 atom clusters.

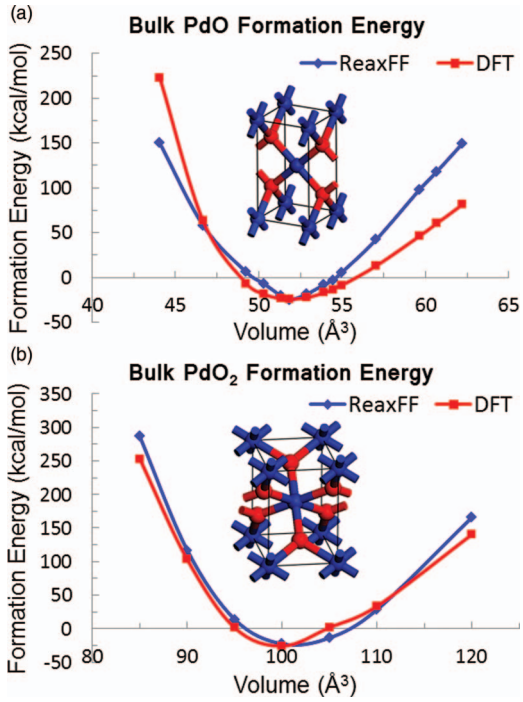

FIG. 3. ReaxFF and DFT expansion-compression curves for (a) PdO and (b) PdO_2. (Insets) Unit cells of PdO and PdO_2.

Expansion-compression curves were obtained for bulk palladium(II) oxide (PdO) and palladium(IV) oxide (PdO_2). The most stable phase, PdO, has a tetragonal lattice with a Pd square-planar oxygen coordination. The experimental lattice constants are $a = b = 3.03$ Å and $c = 5.33$ Å.[93] The PdO_2 phase is thermally unstable under ambient conditions,[94] and is included in the parameterization process to help diversify the DFT training set. To model PdO_2, we constructed an orthogonal unit cell with an octahedral oxygen coordination surrounding each Pd atom. The unit cells for both phases are shown in Figure 3 with the corresponding expansion-compression curves. The results in the figure show good agreement between ReaxFF and DFT. For PdO, ReaxFF predicts equilibrium lattice spacings of $a = b = 3.06$ Å and $c = 5.53$ Å, which agrees with both the DFT values of $a = b = 3.07$ Å and $c = 5.52$ Å, and the experimental values listed above. These lattice constants yield a density of 7.81 g/cm^3, in reasonable agreement with the experimental value of 8.28 g/cm^3. For PdO_2, ReaxFF predicts equilibrium lattice constants of $a = b = 4.62$ Å and $c = 3.24$ Å, which is consistent with the DFT values of $a = b = 4.59$ Å and $c = 3.22$ Å. ReaxFF predicts zero-Kelvin formation energies (calculated relative to Pd–fcc and gas phase O_2) of −25.09 kcal mol^{-1} and −22.63 kcal mol^{-1} for PdO and PdO_2, respectively, which agrees with the respective DFT values of −24.32 kcal mol^{-1} and −25.74 kcal mol^{-1}. This demonstrates that the potential is capable of describing Pd–O interactions in bulk phases near equilibrium densities. Deviation in the PdO energy-volume curve occurs at densities far from equilibrium, where the energies are significantly higher (~35 kcal mol^{-1} or greater) than the equilibrium value. It is more important for ReaxFF to correctly reproduce the equilibrium volume and formation energy. Correspondingly,

TABLE IV. Relative PdO surface energies.

PdO surface	ReaxFF (kcal mol^{-1})	DFT (kcal mol^{-1})
100	4.60	7.01
110	12.27	14.05
111	4.01	6.94
001	12.81	14.65
101	11.45	13.65

deviations at higher energies are acceptable as long as the corresponding energies are high enough to ensure that such structures are not accessible under the simulation conditions of interest.

The ReaxFF potential was also optimized to describe Pd–O interactions in surface structures. First, the parameters were fit to DFT relative surface formation energies for PdO(100), PdO(101), PdO(110), PdO(111), and PdO(001). Relative surface formation energies were calculated with the formula $E_{rel} = E_{slab,(PdO)n}/n - E_{PdO,bulk}$, where $E_{slab,(PdO)n}$ is the energy of the surface slab model consisting of n PdO units and $E_{PdO,bulk}$ is the reference energy of one PdO unit in the optimized bulk PdO structure. In order to use this energy reference, our slab models required stoichiometric amounts of Pd and O. Accordingly, the models feature one Pd-terminated side and one O-terminated side, or one Pd terminated side and one PdO terminated side for the PdO(100) surface; resulting in a surface energy averaged over both Pd and O terminations. The results shown in Table IV demonstrate qualitative agreement between ReaxFF and DFT in predicting the relative stability of each surface. The ReaxFF values for surface energy are linked to bulk formation energies, which causes the accuracy of ReaxFF's description of PdO surface formation energies to trade-off with the accuracy of its description of the PdO bulk formation energy. In this instance, we chose to tolerate the potential's tendency to systematically under predict surface energies in order to correctly predict the bulk oxide formation energy.

The Pd/O interaction parameters were additionally trained against DFT data for oxygen adsorption and dissociation on Pd(111), Pd(110), and Pd(100). Adsorption data for both chemisorbed O_2 molecules and dissociated oxygen atoms were included in the training set. Binding energies were calculated relative to the clean surface and a gas phase O_2 molecule, and were normalized by the number of oxygen atoms in the cell: $E_{bind} = (E_{clean} - E_{O/Pd\text{-}surf})/n_o + 1/2\ E_{O_2}$. The 2 × 2 periodic cells employed resulted in either 0.25 mono-layer, 0.5 mono-layer, or 1.0 mono-layer coverage, depending on the number of adsorbed oxygen atoms contained in the cell. This ensures that the potential can properly describe interactions between adsorbed oxygen atoms on the Pd surface at variable coverages.

The adsorption data presented in Figure 4 demonstrate the feasibility of the ReaxFF potential, which qualitatively reproduces numerous oxygen binding trends predicted by DFT. ReaxFF correctly predicts that oxygen will bind less strongly to both the Pd(111) and Pd(100) surfaces as oxygen coverage increases. For the Pd(111)-fcc site, the ReaxFF binding energy decreases from 29.93 kcal mol^{-1} at 0.25 ML to 23.48 kcal mol^{-1} at 0.5 ML, in agreement with the respective DFT values of 30.05 kcal mol^{-1} and 27.18 kcal mol^{-1}. Similarly for the Pd(111)-hcp site, ReaxFF yields binding energies of 31.20 kcal mol^{-1} at 0.25 ML and 26.82 kcal mol^{-1} at 0.5 ML, which correspond to the DFT values of 25.21 kcal mol^{-1} at 0.25 ML and 23.64 kcal mol^{-1} at 0.5 ML. These numbers are in agreement with DFT energies reported previously by Todorova *et al.*,[95] who calculated binding energies of 34 kcal mol^{-1} and 28 kcal mol^{-1} for the fcc and hcp sites, respectively, at 0.25 ML, and binding energies of 26 kcal mol^{-1} and 21 kcal mol^{-1} at 0.5 ML. On the Pd(100) surface, ReaxFF yields a binding energy of 25.35 kcal mol^{-1} at 0.5 ML and 7.36 kcal mol^{-1} at 1 ML, in agreement with the respective DFT values of 26.75 kcal mol^{-1} and 9.57 kcal mol^{-1}. These energies are also in agreement with the DFT values of 24.7 kcal mol^{-1} and 7.9 kcal mol^{-1} reported by Zhang *et al.*[96] On Pd(111) tetrahedral and octahedral subsurface sites, ReaxFF yields binding energies of −5.90 kcal mol^{-1} and −9.67 kcal mol^{-1}, respectively. This is in qualitative agreement with the respective DFT values of −7.15 kcal mol^{-1} and −15.35 kcal mol^{-1}, as well as the previously reported[97] DFT values of −8.5 kcal mol^{-1} and −17.9 kcal mol^{-1}. For O_2 binding

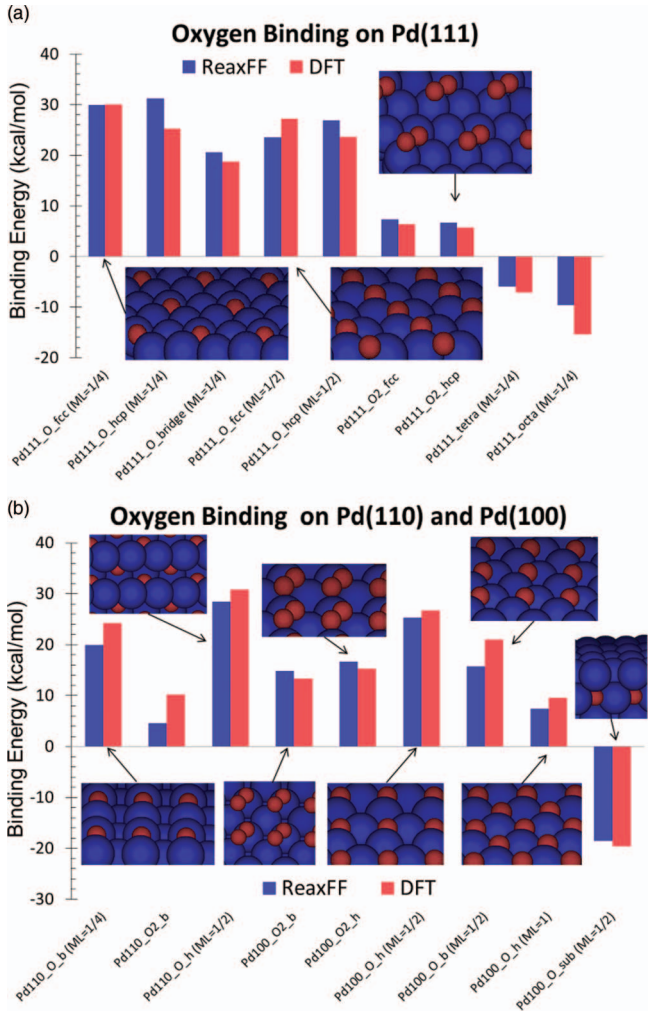

FIG. 4. ReaxFF and DFT surface binding energies for oxygen on (a) Pd(111), (b) Pd(110), and Pd(100). Notation: b = bridge, h = hollow, octa = octahedral subsurface, and tetra = tetrahedral subsurface.

TABLE V. Oxygen binding energies on Pd(111), Pd(100), and Pd(110).

Adsorption site	ReaxFF (kcal mol^{-1})	DFT (kcal mol^{-1})	Literature (kcal mol^{-1})
111-fcc (1/4 ML)	29.93	30.05	34[95]
111-hcp (1/4 ML)	31.20	25.21	28[95]
111-bridge (1/4 ML)	20.55	18.72	22[95]
111-fcc (1/2 ML)	23.48	27.18	26[95]
111-hcp (1/2 ML)	26.82	23.64	21[95]
111-O_2 fcc	7.29	6.29	6.5[98]
111-O_2 hcp	6.64	5.65	6.1[98]
111-tetra (1/4 ML)	− 5.90	− 7.15	−8.5[97]
111-octa (1/4 ML)	− 9.67	− 15.35	−17.9[97]
100-hollow (1/2 ML)	25.35	26.75	24.7[96]
100-hollow (1 ML)	7.36	9.57	7.9[96]
100-bridge (1/2 ML)	15.74	20.98	18.5[96]
100-octa (1/2 ML)	− 18.52	− 19.60	...
100-O_2 bridge	14.83	13.38	...
100-O_2 hollow	16.67	15.34	...
110-bridge (1/4 ML)	19.91	24.21	...
110-hollow (1/2 ML)	28.46	30.79	...
110-O_2 bridge	4.65	10.26	...

on the Pd(111) surface, ReaxFF yields binding energies of 7.29 kcal mol^{-1} and 6.64 kcal mol^{-1} on the fcc and hcp sites, respectively, in agreement the DFT values of 6.29 kcal mol^{-1} and 5.65 kcal mol^{-1}. These numbers are also in agreement with those reported by Honkala *et al.*,[98] who calculated DFT adsorption energies of 6.5 kcal mol^{-1} and 6.1 kcal mol^{-1} for O_2 adsorption on the analogous fcc and hcp sites. These data are summarized in Table V, together with the appropriate literature comparisons where available.

We note that ReaxFF does not correctly reproduce the relative stability of an oxygen atom adsorbed on fcc and hcp sites. This is a result of the weighting scheme used during parameter optimization, which minimizes the overall deviation between DFT and ReaxFF. Here, we prefer that the potential is within ∼5 kcal mol^{-1} for both sites with the reverse stability ordering, as opposed to having the ordering correct with a larger overall deviation. Furthermore, experimental and theoretical examples exist in the literature showing that the hcp site may be preferred over the fcc site, despite contrary DFT evidence. Using ion-scattering experiments, Steltenpohl and Memmel found that the hcp site is preferred over the fcc site.[99] German *et al.* show that the hcp/fcc preference can be dependent on the DFT method and functional employed; they found that the hcp site is ∼3 kcal mol^{-1} more stable than the fcc site when using a converged cluster model of the Pd(111) surface with the PBE0 functional.[100] Still, the majority of evidence in the literature supports the conclusion that the fcc site is preferred, suggesting that these examples are anomalous. Ultimately, training ReaxFF to correctly reproduce the hcp/fcc trend entails a significant increase in the overall deviation between ReaxFF and DFT, which is not justified since the hcp/fcc site preference is not a principle interest of this study.

Finally, the potential was trained to reproduce O_2 dissociation barriers, which were obtained by CI-NEB for both DFT and ReaxFF. The initial and final structures used in the CI-NEB simulations were chosen from high symmetry sites to provide plausible O_2 dissociation paths that could be used to compare analogous DFT and ReaxFF barriers. Figure 5 shows the resulting ReaxFF dissociation paths over the Pd(111), Pd(100), and Pd(110) surfaces, which yield barriers of 19.2 kcal mol^{-1}, 20.4 kcal mol^{-1}, and 17.2 kcal mol^{-1}, respectively. This compares well with our respective DFT barriers of 17.1 kcal mol^{-1}, 17.8 kcal mol^{-1} for Pd(111) and Pd(100); and the barrier of 16 kcal mol^{-1} calculated by Junell *et al.* for Pd(110).[101] The reaction paths over Pd(100) and Pd(110) were not explicitly contained in the training set, demonstrating the transferability of the potential for describing barriers not considered in the training process.

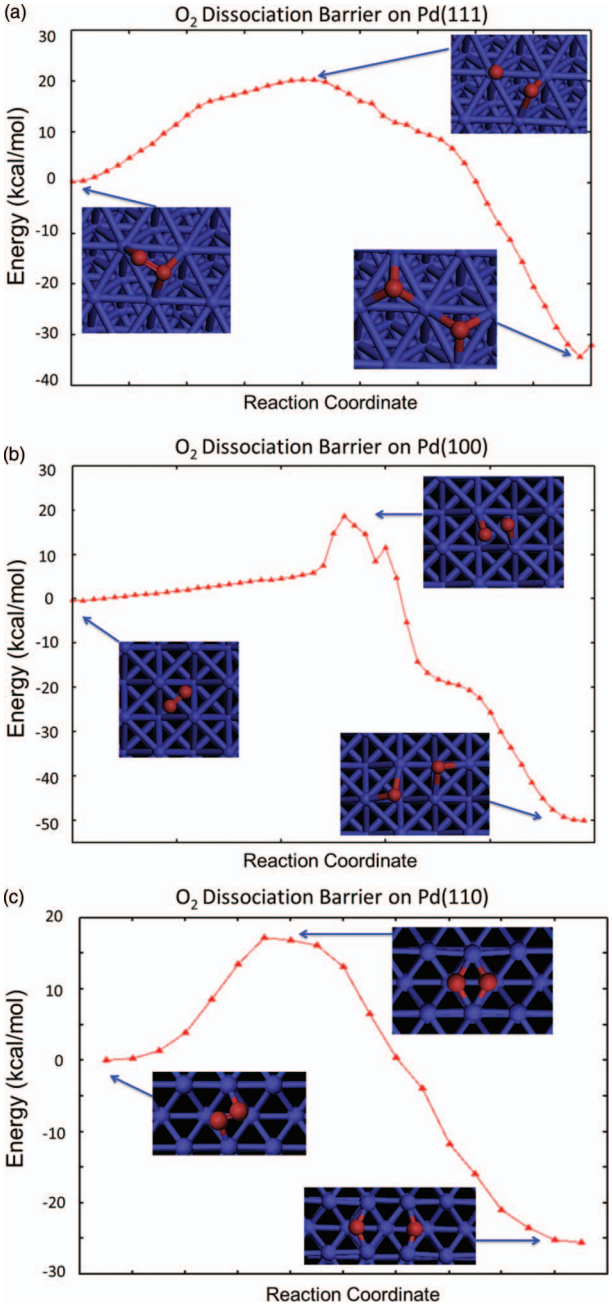

FIG. 5. ReaxFF O_2 dissociation barrier over (a) the Pd(111) surface, (b) the Pd100 surface, and (c) the Pd(110) surface. (Insets) Initial structure, transition state, and final structure.

The entire Pd/O parameter set contained in Table I and the ReaxFF general parameters are provided in ReaxFF input format in the supplementary material.[105]

B. MD simulations of palladium oxide formation

The Pd/O interaction parameters developed above were implemented in 250 ps NVT simulations of oxide formation on Pd surfaces and clusters. The experimental results discussed in the Introduction suggest that oxidation of the bulk below Pd(111)[28] and Pd(100)[22] is kinetically hindered by surface and subsurface oxide phases, whereas Pd(110)[31] readily forms a bulk oxide. We conducted MD simulations to determine if this behavior is reproduced by the ReaxFF Pd/O interaction potential. Pd clusters were also included in the analysis, as many Pd catalysts feature Pd clusters dispersed on oxide supports, rather than perfect single-crystal surfaces. The Pd(111), Pd(110), and Pd(100) surface models consist of periodic surfaces with surface vectors chosen as near to 20 Å × 20 Å as possible depending on Pd–Pd spacing. Each slab model is 10 Pd layers thick, with periodic images in the z-direction separated by 100 Å of vacuum space that is populated with O_2 molecules. Each simulation began with 40 O_2 molecules in the gas phase above the surface. The Pd(111), Pd(100), and Pd(110) slabs consist of 640, 500, and 400 atoms, respectively. The ratio of Pd to O atoms will affect the overall amount of oxygen that can be absorbed by each surface. Since we are interested in comparing oxidation rates, we chose O/Pd ratios that are well below the stoichiometric 1:1 ratio characteristic of bulk PdO, thus ensuring that the metal never becomes saturated with oxygen atoms. This, in conjunction with the high simulation temperatures and pressures, allows us to simulate an oxidation process that is kinetically limited, as opposed to thermodynamically limited. As such, the dimensions of the simulation cells were chosen such that each Pd surface has an equal number of Pd layers exposed to a comparable O_2 environment, allowing for a direct comparison of the relative oxidation kinetics on each surface. The populations of O_2 molecules and O atoms either present in the gas phase, adsorbed on the Pd surface, or absorbed in the bulk were recorded at 25 fs intervals. The resulting species population plots for each simulation are shown in Figure 6 for surface simulations and in Figure 7 for cluster simulations; and the structures of the cluster and surface models are shown in Figures 8 and 9, respectively.

Both temperature-ramp and fixed-temperature simulations were employed to assess reactivity toward O_2 dissociation and oxide formation. In the temperature-ramp simulations, the system temperature was initially set at 500 K and was increased at a rate of 8 K/ps, yielding a final temperature of 2500 K. This results in a pressure range in the gas phase of approximately 15 MPa to 2 MPa depending on the temperature and number of O_2 molecules remaining in the gas phase; a table summarizing approximate pressure variation during the temperature-ramp simulations is provided in the supplementary material.[105] The results in Figures 6 and 7 demonstrate the necessity of high temperature and pressure ranges, as appreciable O_2 dissociation does not occur below ~1000 K and ~7 MPa at these timescales.

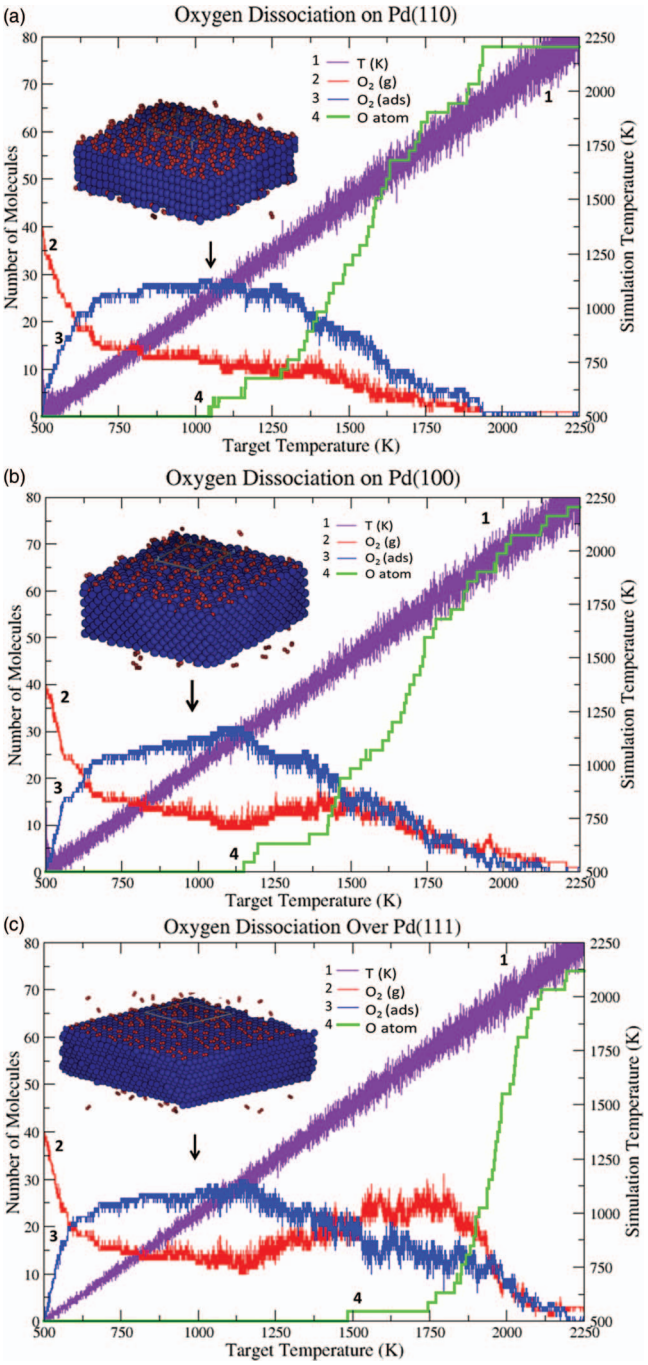

FIG. 6. Temperature ramped NVT simulation of O_2 dissociation and oxide formation on (a) Pd(110), (b) Pd(100), and (c) Pd(111) surfaces. (Insets) Periodic surface structure at 1000 K.

The relative activity of each surface toward oxide formation can be assessed by comparing the onset temperature of oxygen dissociation (T_d) for each surface, marked by the appearance of atomic oxygen. As seen in Figure 6, the Pd(110) surface dissociates oxygen most readily, with T_d = 1040 K compared to T_d = 1150 K for Pd(100) and T_d = 1490 K for Pd(111). On all the surfaces, O_2 adsorbs at low temperatures until the surface becomes saturated, and either dissociates or desorbs back into the gas phase as temperature

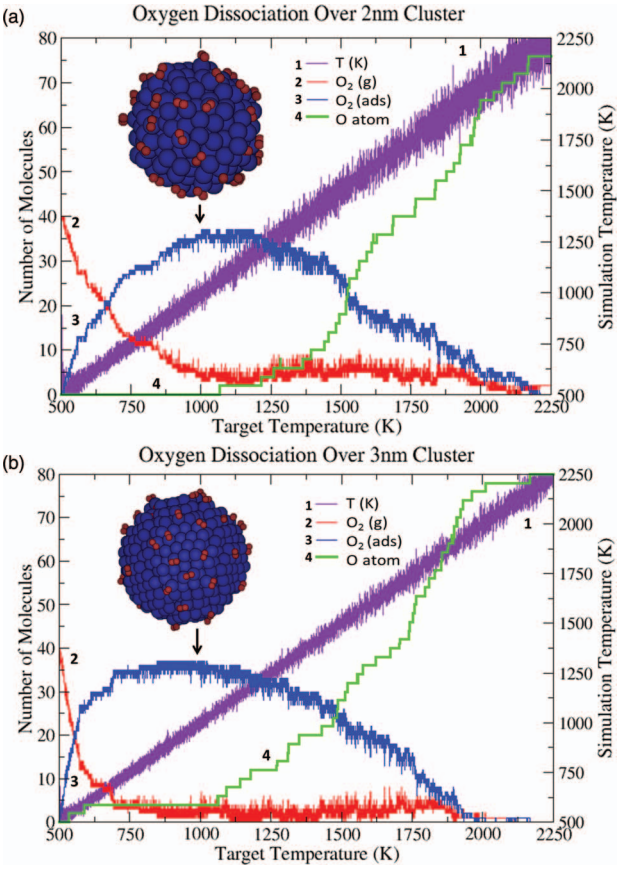

FIG. 7. Temperature ramped NVT simulation of O_2 dissociation and oxide formation on (a) 2-nm diameter Pd_{321} cluster and (b) 3-nm diameter Pd_{935} cluster. (Insets) Surface structure at 1000 K.

increases. The kinetic hindrance of subsurface oxygen migration beneath Pd(111) and Pd(100) surfaces is demonstrated by a pronounced increase in the number of gas phase oxygen molecules as O_2 desorbs back into the gas phase after T_d. This occurs when the surface becomes saturated with oxygen that cannot migrate into the bulk, and therefore desorbs as the temperature increases. Over Pd(110), there is no desorption of O_2 molecules after T_d, indicating that oxygen atoms can rapidly diffuse into the subsurface, thus forming a bulk oxide with little kinetic hindrance in these temperature ranges.

The difference in T_d between the Pd(111) and Pd(100) surface is somewhat surprising given the similar dissociation barriers shown in Figure 5. This difference can be attributed to

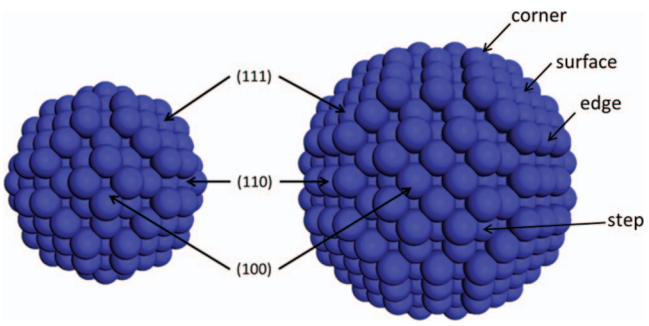

FIG. 8. Structure of the (left) 2-nm and (right) 3-nm Pd clusters.

surface coverage effects. The O_2 dissociation barriers shown in Figure 5 were calculated in a 3 × 3 cell in order to minimize adsorbate-adsorbate interactions affecting the barrier height. These barriers, therefore, correspond to the O_2 activation energy at low coverage. To determine the barriers at higher coverage, we calculated DFT barriers in a 2 × 2 cell to illustrate the effect of surface coverage on barrier heights. The barrier over Pd(111) increases from 17.1 kcal mol^{-1} at 0.22 ML to 25.14 kcal mol^{-1} at 0.5 ML, while the barrier over Pd(100) remains near ∼17 kcal mol^{-1}. Under the simulation conditions presented here, the surface coverage of O_2 prior to the onset of dissociation is high (∼0.5 ML), thus the high coverage barriers are more pertinent for comparing dissociation temperatures. The high coverage barriers for dissociation over Pd(100) and Pd(110) are close in magnitude (both near ∼17 kcal mol^{-1}), and are significantly lower than that over Pd(111) (∼25 kcal mol^{-1}). This explains why dissociation over Pd(110) and Pd(100) begins at similar temperatures (1040 K and 1150 K, respectively) and why Pd(111) has a much higher dissociation temperature (1490 K). A similar trend in coverage dependence was reported for O_2 dissociation on Pt(111) by Miller *et al.*,[102] who found that the O_2 dissociation barrier increased by ∼12 kcal mol^{-1} when the coverage is increased from 0.25 ML to 0.5 ML. Also, similar high coverage barriers over Pd(111) have been reported by Eichler *et al.*[103] (∼23 kcal mol^{-1} at 0.33 ML), and by Honkala *et al.*[98] (∼27 kcal mol^{-1} at 0.5 ML).

Fixed temperature simulations were also conducted to further assess the oxidation affinity of the three Pd surfaces. A temperature of 1400 K was chosen for these simulations, which is high enough to yield oxygen dissociation in the simulation timeframe, but is low enough to maintain a crystalline metal lattice. The results, shown in Figure 9, depict the initial and final structures of each surface after exposure to O_2(g) for the duration of the 250 ps simulation. As seen in Figure 9(a), oxygen dissociates over the Pd(111) surface, but, with little subsurface oxygen migration, does not form a bulk oxide. The Pd(100) surface forms a surface oxide with oxygen migrating into the first two subsurface layers, but maintains a pure Pd crystal structure in the bulk. Oxygen rapidly dissociates and migrates into the subsurface over the Pd(110) surface, resulting in a bulk oxide with no crystalline Pd structure remaining in the bulk. The migration of oxygen into the Pd(110) sublayers leads to a transition in the lattice structure of the bulk, yielding the disordered phase seen in the figure. The fixed cell dimension prohibits the system from relaxing into an ordered PdO crystalline structure. This result demonstrates that the surface structure of crystalline Pd(110) allows oxygen atoms to migrate into the subsurface, which is not seen under comparable conditions for Pd(111) and Pd(100). This trend is the result of two factors. First, the oxygen dissociation barrier is lower over Pd(110) compared to the other two surfaces, which is reflected in the lower value for T_d discussed above. Second, oxygen diffusion into the bulk occurs more rapidly over Pd(110) due to wide surface channels present on the Pd(110) surface, which are easily penetrated by diffusing oxygen compared to the close packed Pd(111) and Pd(100) surfaces.

Additionally, we calculated barriers for O atoms to migrate from a surface hollow site to a subsurface octahedral

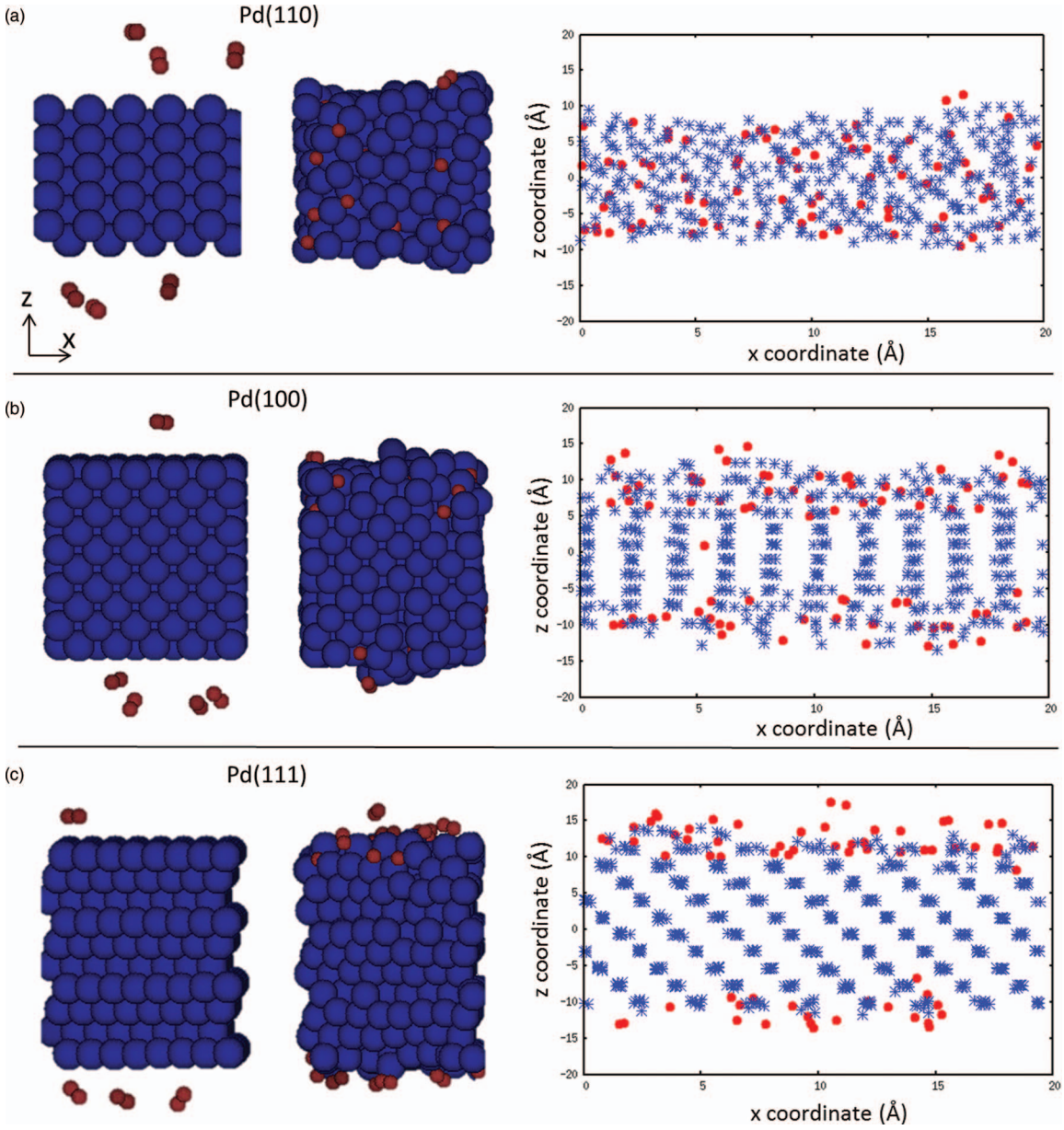

FIG. 9. NVT simulation of O_2 dissociation at 1400 K on (a) Pd(110), (b) Pd(100), and (c) Pd(111) surfaces. The initial structures are shown on the left and the final structures after 250 ps are shown on the right (note: not all gas phase atoms are shown). Plots represent the final x and z coordinates of all atoms in the system (red dots = oxygen atoms and blue stars = Pd atoms).

site over each surface. On the Pd(111) surface, ReaxFF yields a barrier of 65 kcal mol^{-1} for an oxygen atom to migrate from a surface fcc site to a subsurface octahedral site, which is in reasonable agreement with the analogous DFT barrier of 58 kcal mol^{-1} (calculated in a 2 × 2 periodic cell). On the Pd(100) and Pd(110) surfaces, the ReaxFF barriers are significantly lower for subsurface migration to octahedral sites at 44 kcal mol^{-1} and 32 kcal mol^{-1}, respectively. This trend is in agreement with the MD results showing that oxygen can diffuse more readily into the Pd(110) surface compared to the Pd(100) and Pd(111) surfaces. These results corroborate the experimental finding, reported by Han *et al.*,[34,35] that Pd(110) has a lower subsurface diffusion barrier than Pd(100) and Pd(111).

Since most catalytic applications feature supported metal particles, rather than single crystal surfaces, we conducted similar temperature-ramp NVT analyses of oxidation on Pd clusters. The cluster simulations were conducted with spherical 2-nm diameter (321 atoms) and 3-nm diameter (935 atoms) cluster models constructed from the bulk-fcc phase, which are shown in Figure 8. As seen in the figure, both clusters feature significant Pd(111), Pd(100), and Pd(110) facets, as well as numerous step, corner, and edge sites. The structural details of each cluster are summarized in Table VI. Each cluster was placed in a 50 Å × 50 Å × 50 Å periodic box with the remaining vacuum space occupied by 40 O_2 molecules. The results, shown in Figure 7, show that the 2-nm cluster begins to dissociate O_2 at 1070 K and allows a negligible

TABLE VI. Structural properties of 3-nm and 2-nm Pd clusters.

3-nm cluster	111	110	100
No. of facets	8	12	6
Area (per facet, Å^2)	82.57	44.67	55.33
Surface atoms (per facet)	7	1	4
Edge atoms (per facet)	3-(100), 3-(110)	2-(111), 2-(100)	…
Corner atoms (per facet)	6	4	8
Step sites (per facet)	…	…	12
2-nm cluster	111	110	100
No. of facets	8	12	6
Area (per facet, Å^2)	44.73	7.95	11.17
Surface atoms (per facet)	3	…	…
Edge atoms (per facet)	3-(100)	…	…
Corner atoms (per facet)	6	4	4
Step sites (per facet)	…	…	8

amount of oxygen molecules to desorb back to the gas phase at high temperatures. Similar results are found for the 3-nm cluster, which begins to rapidly dissociate O_2 at 1060 K and does not allow oxygen to desorb from the surface. This is qualitatively comparable to the performance of the Pd(110) surface, suggesting that oxide diffusion into the bulk is less kinetically hindered on clusters in this size range than for close packed single-crystal surfaces under comparable temperature and pressure conditions. Similar to the Pd(110) surface, rapid oxidation in the bulk phase is the result of two factors. First, the cluster surfaces contain under-coordinated Pd atoms on corner, step, and edge sites resulting in low O_2 dissociation barriers, allowing the surface to rapidly saturate with oxygen atoms. For example, we calculated a ReaxFF dissociation barrier of 12 kcal mol^{-1} over a corner site on the 2-nm cluster, which is even lower than the dissociation barrier over Pd(110). Second, the cluster surface is less closely packed, allowing oxygen atoms to readily diffuse into the bulk. Here, we calculated a subsurface migration barrier from a step site to a subsurface octahedral site of 26 kcal mol^{-1}, which again is significantly lower than the analogous barrier on the single-crystal surfaces.

The kinetic behavior observed in these MD simulations suggests that surface oxide phases do not limit bulk oxidation in clusters at high temperatures. These results, however, are limited to high temperatures and pressures to allow oxidation to occur on an accessible timescale. As such, the results cannot conclusively demonstrate a lack of kinetic hindrance for the analogous process at low temperatures. Nevertheless, the MD simulations suggest that oxidation over clusters is qualitatively similar to the Pd(110) surface, which is experimentally[31] shown to form a bulk oxide without kinetic hindrance. It is therefore important to also assess the thermodynamic stability of bulk and surface oxide phases over Pd clusters at lower temperatures and pressures, which is addressed in Sec. III C.

C. Grand canonical Monte Carlo simulations of palladium oxide formation

The MD results in Sec. III B underscore the importance of investigating the thermodynamic stability of oxide formations in Pd clusters at temperatures and pressures typically employed during oxidation catalysis. For this reason, we applied a hybrid GC-MC/MD method to determine the extent of surface and bulk oxidation in Pd clusters as a function of temperature and oxygen partial pressure. Each simulation began with a 3-nm diameter Pd_{935} cluster in a 50 Å × 50 Å × 50 Å box. Oxygen atoms were added, moved, and removed from the system until the energy of the system converged such that the total system energy varied less than 20 kcal mol^{-1} over the final 1000 MC trial moves. This is demonstrated in Figure 10, which depicts the convergence of both oxygen concentration and system energy (calculated relative to the clean Pd cluster and the oxygen chemical potential) for simulations at 500 K with varying oxygen pressures. As seen in the figure, the number of MC iterations (defined as an attempted move, as opposed to an accepted move) required to reach equilibration is typically between 15 000 and 25 000 for this system, depending on temperature and pressure. An example video of a GC-MC/MD simulation of oxide formation over a 3-nm particle at 1 atm and 300 K is provided in the supplementary material.[105]

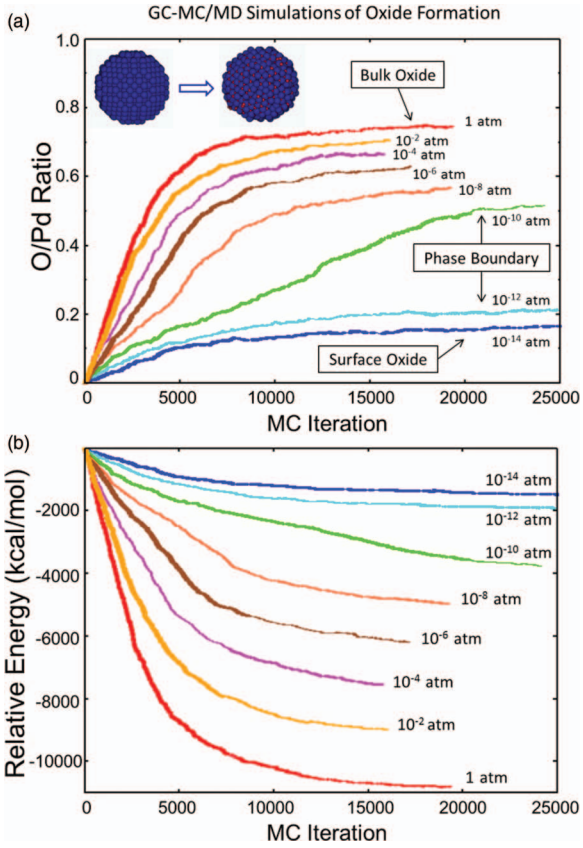

FIG. 10. (a) Ratio of oxygen to palladium atoms and (b) relative energy ($E_{relative} = E_{system,n_o} - E_{clean} - n_o\mu_{ref}$) of the system during a grand canonical Monte Carlo simulation of PdO formation on a 3-nm diameter Pd_{935} cluster at $T = 500$ K and $P = 10^{-14}$ atm (dark blue), $P = 10^{-12}$ atm (light blue), $P = 10^{-10}$ atm (green), $P = 10^{-8}$ atm (orange), $P = 10^{-6}$ atm (brown), $P = 10^{-4}$ atm (magenta), $P = 10^{-2}$ atm (yellow), and $P = 1$ atm (red). (Insets) Initial and final structure after GC-MC at 500 K and 1 atm.

A total of 34 GC-MC/MD simulations were conducted to sample the oxidation phase space at temperatures ranging from 300 K to 1300 K and oxygen pressures ranging

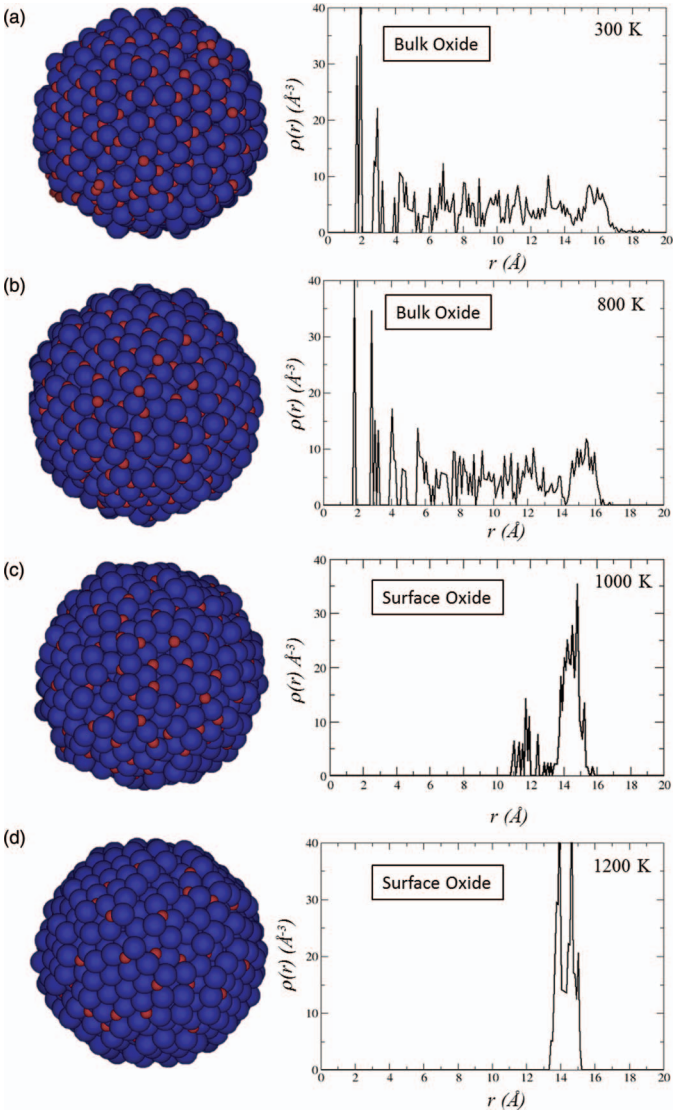

FIG. 11. Final structure and radial distribution of oxygen atoms relative to the center of the Pd cluster after grand canonical Monte Carlo simulations of oxide formation at $P = 1$ atm and $T =$ (a) 300 K, (b) 800 K, (c) 1000 K, and (d) 1200 K.

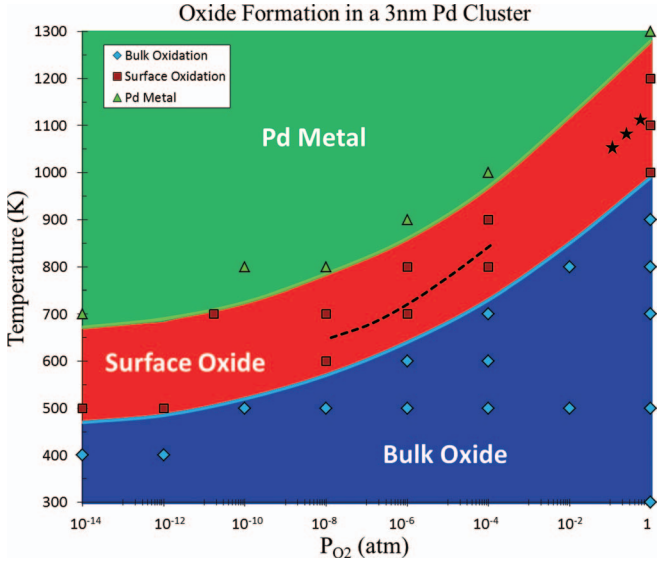

FIG. 12. Phase diagram derived from ReaxFF GC-MC/MD simulations of oxide formation in a 3-nm diameter Pd cluster. The points indicate the temperature and pressure of each GC-MC simulation, from which the phase boundaries are estimated. The dashed black line indicates the bulk Pd → PdO transition reproduced from Ref. 28, which was calculated from experimental enthalpies and heat capacities. The stars indicate experimentally observed bulk Pd → PdO transitions at 0.1 atm/1050 K, 0.5 atm/1085 K, and 0.9 atm/1125 K.[104]

from 10^{-14} atm to 1 atm. The degree of oxidation was determined by the final O/Pd ratio of the equilibrated system. As expected, the O/Pd ratio decreases as the oxygen pressure is lowered, and increases as the temperature is lowered. Figure 10 shows a clear distinction between bulk and surface oxidation, indicated by the pronounced increase in converged O/Pd ratios that occurs between 10^{-10} atm and 10^{-12} atm. To further analyze the structure of the oxide phases, we used the atomic coordinates of the equilibrated systems to calculate the radial distribution of oxygen atoms in the cluster. By analyzing the radial distribution of oxygen atoms in the cluster, we determined whether oxidation occurred primarily on the particle surface or throughout the particle bulk. This is demonstrated in Figure 11, which shows the final structure and corresponding radial distribution of oxygen atoms from the center of the cluster ($r = 0$) at 1 atm over a range of temperatures. As seen in Figures 11(a) and 11(b), simulations under oxidizing conditions (300–800 K, 1 atm) yield a nearly uniform oxygen density throughout the particle. Figure 11(d) shows the oxygen distribution at 1 atm and 1200 K, where oxygen atoms adsorb on the surface, but not in the bulk. Figure 11(c) shows the onset of bulk oxidation at 1000 K and 1 atm, which lies near the phase boundary between bulk and surface oxidation. We used similar plots (available in the supplementary material[105]) to classify the final structure of each MC simulation as (1) bulk oxide, (2) surface oxide, or (3) Pd metal. Surface oxides were defined broadly to include varying coverages of chemisorbed oxygen. Adsorbed oxygen atoms almost always rearranged surface Pd atoms forming a surface oxide, so we did not differentiate between surface adsorption and surface oxidation. These distinctions were used to estimate the boundaries of an oxidation phase diagram, shown in Figure 12, which predicts the *T*,*P* regions in which a surface oxide phase is thermodynamically stable on a 3-nm Pd cluster.

The phase boundaries predicted by the ReaxFF GC-MC/MD method for the 3-nm cluster are similar to the experimental and *ab initio* phase diagrams for the Pd(111) surface determined by Ketteler *et al.*[28] and for the Pd(100) surface determined by Lundgren *et al.*[22] Both contain thermodynamically stable surface oxide phases in *T*,*P* regions similar to those predicted by ReaxFF. The phase diagram derived from the ReaxFF GC-MC method also compares favorably with experimentally observed bulk Pd → PdO phase boundaries. These comparisons are demonstrated by the dotted black line in Figure 12, which represents the bulk Pd → PdO phase boundary derived by Ketteler *et al.*[28] from experimental enthalpies and heat capacities. Additionally, the ReaxFF phase diagram is in agreement with bulk Pd → PdO phase transitions observed experimentally by Zhang *et al.*, which are marked in Figure 12 by black stars.[104] The uncertainty

introduced by the inaccuracy of DFT for describing O_2 systematically shifts the GC-MC/MD boundaries to lower temperatures; the actual boundary may lie at higher temperatures. This indicates that the cluster forms an oxide more readily than the single crystal surfaces and the Pd bulk, which is expected since the cluster surface exposes under-coordinated Pd atoms at corner and edge sites that serve as nucleation sites for oxide growth. The agreement between experimental, *ab initio*, and ReaxFF phase diagrams validates the Pd/O interaction potential, and demonstrates the applicability of the hybrid MD/GC-MC method for assessing the thermodynamic properties of large (∼1000 atom), non-periodic systems.

IV. CONCLUSION

Oxide formation on noble metal surfaces, such as palladium, plays an important role in numerous industrial catalytic operations. To investigate the dynamics of oxidation processes on Pd surfaces and clusters, we derived a ReaxFF interaction potential for Pd/O from an extensive set of DFT data for both bulk and surface properties. Using this potential, we conducted NVT molecular dynamics simulations of oxide formation on Pd(111), Pd(110), and Pd(100). These results, while limited to high temperatures, are in agreement with previous experimental observations,[34] predicting that oxygen migration into the subsurface of Pd(110) is less kinetically hindered than Pd(111) and Pd(100). Our MD results similarly suggest that oxide formation in Pd clusters is qualitatively comparable to Pd(110); although the lack of kinetic hindrance in clusters cannot be conclusively demonstrated by high temperature simulations. Building on this kinetic result, we introduced a hybrid GC-MC/MD approach to assess the thermodynamic stability of oxide formation on Pd clusters. Using this method, we derived a theoretical phase diagram for oxidation in spherical 3-nm diameter Pd_{935} clusters. The corroboration between experiment and ReaxFF both validates the Pd/O interaction potential, and demonstrates the feasibility of the hybrid GC-MC/MD method. The formalism of the hybrid GC-MC/MD method is transferrable to other multi-component systems, and is capable of deriving theoretical phase diagrams that are either in temperature and pressure ranges inaccessible to experimental methods, or are too large or irregular to treat with *ab initio* methods in a computationally tractable timescale.

ACKNOWLEDGMENTS

This research was supported by funding from the National Science Foundation Grant No. CBET-1032979. R.J.M. acknowledges funding from NSF Grant No. CHEM-1026717.

[1]E. Lundgren, G. Kresse, C. Klein, M. Borg, J. N. Andersen, M. De Santis, Y. Gauthier, C. Konvicka, M. Schmid, and P. Varga, Phys. Rev. Lett. **88**(24), 246103 (2002).
[2]W. X. Li, L. Österlund, E. K. Vestergaard, R. T. Vang, J. Matthiesen, T. M. Pedersen, E. Lægsgaard, B. Hammer, and F. Besenbacher, Phys. Rev. Lett. **93**(14), 146104 (2004).
[3]J. Gustafson, A. Mikkelsen, M. Borg, J. N. Andersen, E. Lundgren, C. Klein, W. Hofer, M. Schmid, P. Varga, L. Köhler, G. Kresse, N. Kasper, A. Stierle, and H. Dosch, Phys. Rev. B **71**(11), 115442 (2005).
[4]P. Kostelník, N. Seriani, G. Kresse, A. Mikkelsen, E. Lundgren, V. Blum, T. Šikola, P. Varga, and M. Schmid, Surf. Sci. **601**(6), 1574–1581 (2007).
[5]C. Dri, C. Africh, F. Esch, G. Comelli, O. Dubay, L. Kohler, F. Mittendorfer, G. Kresse, P. Dudin, and M. Kiskinova, J. Chem. Phys. **125**(9), 094701 (2006).
[6]J. Klikovits, M. Schmid, L. R. Merte, P. Varga, R. Westerström, A. Resta, J. N. Andersen, J. Gustafson, A. Mikkelsen, E. Lundgren, F. Mittendorfer, and G. Kresse, Phys. Rev. Lett. **101**(26), 266104 (2008).
[7]J. Klikovits, E. Napetschnig, M. Schmid, N. Seriani, O. Dubay, G. Kresse, and P. Varga, Phys. Rev. B **76**(4), 045405 (2007).
[8]H. W. Jen, G. W. Graham, W. Chun, R. W. McCabe, J. P. Cuif, S. E. Deutsch, and O. Touret, Catal. Today **50**(2), 309–328 (1999).
[9]H. S. Gandhi, G. W. Graham, and R. W. McCabe, J. Catal. **216**(1–2), 433–442 (2003).
[10]T. Kobayashi, T. Yamada, and K. Kayano, Appl. Catal., B **30**(3–4), 287–292 (2001).
[11]M.-F. Luo, Z.-Y. Hou, X.-X. Yuan, and X.-M. Zheng, Catal. Lett. **50**(3), 205–209 (1998).
[12]T. Engel and G. Ertl, J. Chem. Phys. **69**(3), 1267–1281 (1978).
[13]B. C. Sales, J. E. Turner, and M. B. Maple, Surf. Sci. **114**(2–3), 381–394 (1982).
[14]E. M. Stuve, R. J. Madix and C. R. Brundle, Surf. Sci. **146**(1), 155–178 (1984).
[15]Y. Xu, J. Q. Ma, Y. F. Xu, L. Xu, H. X. Li, and H. Li, RSC Adv. **3**(3), 851–858 (2013).
[16]R. Toyoshima, M. Yoshida, Y. Monya, K. Suzuki, B. S. Mun, K. Amemiya, K. Mase, and H. Kondoh, J. Phys. Chem. Lett. **3**(21), 3182–3187 (2012).
[17]G. B. Hoflund, H. A. E. Hagelin, J. F. Weaver, and G. N. Salaita, Appl. Surf. Sci. **205**(1–4), 102–112 (2003).
[18]J. F. Weaver, J. A. Hinojosa Jr., C. Hakanoglu, A. Antony, J. M. Hawkins, and A. Asthagiri, Catal. Today **160**(1), 213–227 (2011).
[19]A. D. Mayernick and M. J. Janik, J. Phys. Chem. C **112**(38), 14955–14964 (2008).
[20]A. D. Mayernick and M. J. Janik, J. Catal. **278**(1), 16–25 (2011).
[21]M. Li, D. Weng, X. D. Wu, J. Wan, and B. Wang, Catal. Today **201**, 19–24 (2013).
[22]E. Lundgren, J. Gustafson, A. Mikkelsen, J. N. Andersen, A. Stierle, H. Dosch, M. Todorova, J. Rogal, K. Reuter, and M. Scheffler, Phys. Rev. Lett. **92**(4), 046101 (2004).
[23]J. Rogal, K. Reuter, and M. Scheffler, Phys. Rev. B **69**(7), 075421 (2004).
[24]M. Todorova, E. Lundgren, V. Blum, A. Mikkelsen, S. Gray, J. Gustafson, M. Borg, J. Rogal, K. Reuter, J. N. Andersen, and M. Scheffler, Surf. Sci. **541**(1–3), 101–112 (2003).
[25]E. H. Voogt, A. J. M. Mens, O. L. J. Gijzeman, and J. W. Geus, Surf. Sci. **373**(2–3), 210–220 (1997).
[26]G. Zheng and E. I. Altman, Surf. Sci. **462**(1–3), 151–168 (2000).
[27]G. Zheng and E. I. Altman, Surf. Sci. **504**(1–3), 253–270 (2002).
[28]G. Ketteler, D. F. Ogletree, H. Bluhm, H. J. Liu, E. L. D. Hebenstreit, and M. Salmeron, J. Am. Chem. Soc. **127**(51), 18269–18273 (2005).
[29]J. A. Hinojosa, Jr. and J. F. Weaver, Surf. Sci. **605**(19–20), 1797–1806 (2011).
[30]H. H. Kan, R. B. Shumbera, and J. F. Weaver, Surf. Sci. **602**(7), 1337–1346 (2008).
[31]R. Westerström, C. J. Weststrate, J. Gustafson, A. Mikkelsen, J. Schnadt, J. N. Andersen, E. Lundgren, N. Seriani, F. Mittendorfer, G. Kresse, and A. Stierle, Phys. Rev. B **80**(12), 125431 (2009).
[32]N. Seriani, J. Harl, F. Mittendorfer, and G. Kresse, J. Chem. Phys. **131**(5), 054701 (2009).
[33]H. Gabasch, W. Unterberger, K. Hayek, B. Klotzer, E. Kleimenov, D. Teschner, S. Zafeiratos, M. Havecker, A. Knop-Gericke, R. Schlogl, J. Y. Han, F. H. Ribeiro, B. Aszalos-Kiss, T. Curtin, and D. Zemlyanov, Surf. Sci. **600**(15), 2980–2989 (2006).
[34]J. Y. Han, D. Y. Zemlyanov, and F. H. Ribeiro, Surf. Sci. **600**(13), 2752–2761 (2006).
[35]J. Y. Han, D. Y. Zemlyanov, and F. H. Ribeiro, Surf. Sci. **600**(13), 2730–2744 (2006).
[36]K. Reuter and M. Scheffler, Phys. Rev. Lett. **90**(4), 046103 (2003).
[37]K. Reuter, D. Frenkel, and M. Scheffler, Phys. Rev. Lett. **93**(11), 116105 (2004).
[38]K. Reuter and M. Scheffler, Phys. Rev. B **68**(4), 045407 (2003).
[39]K. Reuter and M. Scheffler, Phys. Rev. B **65**(3), 035406 (2001).
[40]J. Tersoff, Phys. Rev. Lett. **61**(25), 2879–2882 (1988).
[41]D. W. Brenner, Phys. Rev. B **42**(15), 9458–9471 (1990).

[42]A. C. T. van Duin, S. Dasgupta, F. Lorant, and W. A. Goddard III, J. Phys. Chem. A **105**(41), 9396–9409 (2001).
[43]K. Chenoweth, A. C. T. van Duin, and W. A. Goddard, J. Phys. Chem. A **112**(5), 1040–1053 (2008).
[44]K. D. Nielson, A. C. T. van Duin, J. Oxgaard, W.-Q. Deng, and W. A. Goddard, J. Phys. Chem. A **109**(3), 493–499 (2005).
[45]J. Ludwig, D. G. Vlachos, A. C. T. van Duin, and W. A. Goddard, J. Phys. Chem. B **110**(9), 4274–4282 (2006).
[46]C. F. Sanz-Navarro, P.-O. Astrand, D. Chen, M. Ronning, A. C. T. van Duin, T. Jacob, and W. A. Goddard, J. Phys. Chem. A **112**(7), 1392–1402 (2008).
[47]C. F. Sanz-Navarro, P.-O. Åstrand, D. Chen, M. Rønning, A. C. T. van Duin, and W. A. Goddard, J. Phys. Chem. C **114**(8), 3522–3530 (2010).
[48]M. R. LaBrosse, J. K. Johnson, and A. C. T. van Duin, J. Phys. Chem. A **114**(18), 5855–5861 (2010).
[49]A. C. T. van Duin, V. S. Bryantsev, M. S. Diallo, W. A. Goddard, O. Rahaman, D. J. Doren, D. Raymand, and K. Hermansson, J. Phys. Chem. A **114**(35), 9507–9514 (2010).
[50]T. T. Järvi, A. C. T. van Duin, K. Nordlund, and W. A. Goddard, J. Phys. Chem. A **115**(37), 10315–10322 (2011).
[51]J. E. Mueller, A. C. T. van Duin, and W. A. Goddard, J. Phys. Chem. C **114**(11), 4939–4949 (2010).
[52]J. E. Mueller, A. C. T. van Duin, and W. A. Goddard, J. Phys. Chem. C **114**(12), 5675–5685 (2010).
[53]A. C. T. van Duin, A. Strachan, S. Stewman, Q. Zhang, X. Xu, and W. A. Goddard, J. Phys. Chem. A **107** (19), 3803–3811 (2003).
[54]J. Quenneville, R. S. Taylor, and A. C. T. van Duin, J. Phys. Chem. C **114**(44), 18894–18902 (2010).
[55]A. C. T. van Duin, B. V. Merinov, S. S. Jang, and W. A. Goddard, J. Phys. Chem. A **112**(14), 3133–3140 (2008).
[56]A. C. T. van Duin, B. V. Merinov, S. S. Han, C. O. Dorso, and W. A. Goddard, J. Phys. Chem. A **112**(45), 11414–11422 (2008).
[57]M. Aryanpour, A. C. T. van Duin, and J. D. Kubicki, J. Phys. Chem. A **114**(21), 6298–6307 (2010).
[58]S. Monti, A. C. T. van Duin, S.-Y. Kim, and V. Barone, J. Phys. Chem. C **116**(8), 5141–5150 (2012).
[59]S. C. James, J. Hamilton, and W. G. Wolfer, Chem. Eng. Sci. **68**(1), 250–257 (2012).
[60]M. W. Lee, R. J. Wolf, and J. R. Ray, J. Alloys Compd. **231**(1–2), 343–346 (1995).
[61]R. J. Wolf, M. W. Lee, R. C. Davis, P. J. Fay, and J. R. Ray, Phys. Rev. B **48**(17), 12415–12418 (1993).
[62]R. J. Wolf, M. W. Lee, and J. R. Ray, Phys. Rev. Lett. **73**(4), 557–560 (1994).
[63]V. Lachet, A. Boutin, B. Tavitian, and A. H. Fuchs, Faraday Discuss. **106**(0), 307–323 (1997).
[64]M. Ruda, E. A. Crespo, and S. R. d. Debiaggi, J. Alloys Compd. **495**(2), 471–475 (2010).
[65]P. Valentini, T. E. Schwartzentruber, and I. Cozmuta, Surf. Sci. **605**(23–24), 1941–1950 (2011).
[66]S. Duane, A. D. Kennedy, B. J. Pendleton, and D. Roweth, Phys. Lett. B **195**(2), 216–222 (1987).
[67]U. H. E. Hansmann, Y. Okamoto, and F. Eisenmenger, Chem. Phys. Lett. **259**(3–4), 321–330 (1996).
[68]B. Mehlig, D. W. Heermann, and B. M. Forrest, Phys. Rev. B **45**(2), 679–685 (1992).
[69]B. M. Forrest and U. W. Suter, Mol. Phys. **82**(2), 393–410 (1994).
[70]K. Chenoweth, A. C. T. van Duin, and W. A. Goddard III, Angew. Chem. Int. Ed. **48**(41), 7630–7634 (2009).
[71]W. J. Mortier, S. K. Ghosh, and S. Shankar, J. Am. Chem. Soc. **108**(15), 4315–4320 (1986).
[72]A. C. T. van Duin, J. M. A. Baas, and B. van de Graaf, J. Chem. Soc., Faraday Trans. **90**(19), 2881–2895 (1994).
[73]D. Raymand, A. C. T. van Duin, M. Baudin, and K. Hermansson, Surf. Sci. **602**(5), 1020–1031 (2008).
[74]N. Metropolis, A. W. Rosenbluth, M. N. Rosenbluth, A. H. Teller, and E. Teller, J. Chem. Phys. **21**(6), 1087–1092 (1953).
[75]D. Frenkel and B. Smit, *Understanding Molecular Simulation: From Algorithms to Applications* (Academic Press, San Diego, 2002).
[76]M. W. Chase and National Institute of Standards and Technology, *NIST-JANAF Thermochemical Tables* (American Chemical Society, Washington, D.C., 1998).
[77]L. Verlet, Phys. Rev. **159**(1), 98–103 (1967).
[78]H. J. C. Berendsen, J. P. M. Postma, W. F. v. Gunsteren, A. DiNola, and J. R. Haak, J. Chem. Phys. **81**(8), 3684–3690 (1984).
[79]G. Kresse and J. Furthmuller, Comput. Mater. Sci. **6**, 15–50 (1996).
[80]G. Kresse and J. Furthmuller, Phys. Rev. B **54** (16), 11169–11186 (1996).
[81]J. P. Perdew, J. A. Chevary, S. H. Vosko, K. A. Jackson, M. R. Pederson, D. J. Singh, and C. Fiolhais, Phys. Rev. B **46**(11), 6671 (1992).
[82]G. Kresse and D. Joubert, Phys. Rev. B **59**(3), 1758–1775 (1999).
[83]H. J. Monkhorst and J. D. Pack, Phys. Rev. B **13**(12), 5188–5192 (1976).
[84]G. Henkelman, B. P. Uberuaga, and H. Jonsson, J. Chem. Phys. **113**(22), 9901–9904 (2000).
[85]J. H. Li, Y. Kong, H. B. Guo, S. H. Liang, and B. X. Liu, Phys. Rev. B **76**(10), 104101 (2007).
[86]D. R. Lide, *Handbook of Chemistry and Physics: A Ready Reference Book of Chemical and Physical Data* (CRC Press, New York, 2004).
[87]C. Kittel, *Introduction to Solid State Physics* (Wiley, Hoboken, NJ, 2013).
[88]F. Birch, Phys. Rev. **71**(11), 809–824 (1947).
[89]N. E. Singh-Miller and N. Marzari, Phys. Rev. B **80**(23), 235407 (2009).
[90]S. M. Foiles, M. I. Baskes, and M. S. Daw, Phys. Rev. B **33**(12), 7983–7991 (1986).
[91]A. Seeger, *International Conference on Vacancies and Interstitials in Metals* (North Holland Pub. Co., Amsterdam, 1970).
[92]D. Raymand, A. C. T. van Duin, D. Spångberg, W. A. Goddard III, and K. Hermansson, Surf. Sci. **604**(9–10), 741–752 (2010).
[93]A. G. Christy and S. M. Clark, Phys. Rev. B **52**(13), 9259–9265 (1995).
[94]S. F. Matar, G. Demazeau, M. H. Möller, and R. Pöttgen, Chem. Phys. Lett. **508**(4–6), 215–218 (2011).
[95]M. Todorova, K. Reuter, and M. Scheffler, J. Phys. Chem. B **108**(38), 14477–14483 (2004).
[96]Y. Zhang, V. Blum, and K. Reuter, Phys. Rev. B **75**(23), 235406 (2007).
[97]M. Todorova, K. Reuter, and M. Scheffler, Phys. Rev. B **71**(19), 195403 (2005).
[98]K. Honkala and K. Laasonen, J. Chem. Phys. **115**(5), 2297–2302 (2001).
[99]A. Steltenpohl and N. Memmel, Surf. Sci. **443**(1–2), 13–18 (1999).
[100]E. D. German, M. Sheintuch, and A. M. Kuznetsov, J. Phys. Chem. C **113**(34), 15326–15336 (2009).
[101]P. Junell, K. Honkala, M. Hirsimäki, M. Valden, and K. Laasonen, Surf. Sci. **546**(2–3), L797–L802 (2003).
[102]D. J. Miller, H. Oberg, L. A. Naslund, T. Anniyev, H. Ogasawara, L. G. M. Pettersson, and A. Nilsson, J. Chem. Phys. **133**(22), 224701–224707 (2010).
[103]A. Eichler, F. Mittendorfer, and J. Hafner, Phys. Rev. B **62**(7), 4744–4755 (2000).
[104]H. Zhang, J. Gromek, G. Fernando, H. Marcus, and S. Boorse, J. Phase Equilib. Diffus. **23**(3), 246–248 (2002).
[105]See supplementary material at http://dx.doi.org/10.1063/1.4815820 for a full Pd/O force-field parameter set in ReaxFF input format; a table of approxiamte MD simultion pressures; GC-MC/MD oxygen radial distribution plots; and an example video of a GC-MC/MD simulation of oxide formation over a 3-nm Pd cluster.